Micromechanical analysis of alkali-activated fly ash-slag paste subjected to elevated temperatures

Wenlin Tu [a], Guohao Fang [b,*], Biqin Dong [c], Mingzhong Zhang [a,*]

[a] Department of Civil, Environmental and Geomatic Engineering, University College London, London, WC1E 6BT, UK

[b] Institute for Advanced Study, Shenzhen University, Shenzhen, 518060, China

[c] School of Civil Engineering, Guangdong Province Key Laboratory of Durability for Marine Civil Engineering, The Key Laboratory on Durability of Civil Engineering in Shenzhen, Shenzhen University, Shenzhen, 518060, China

Abstract: To advance the development of high-temperature/fire-resistant alkali-activated materials, it is vital to understand their behaviour subjected to elevated temperatures. This paper presents a systematic experimental study on microstructural characteristics and micromechanical properties of alkali-activated fly ash-slag paste (AAFS) after exposure to 20-800 ºC. The microstructural evolution in terms of morphology, phase assemblage and gel compositions was examined using backscattered scanning electron microscope-energy dispersive spectrometry (BSEM-EDS), while atomic force microscopy (AFM) and nanoindentation tests were conducted to evaluate the micromechanical properties at elevated temperatures. Results indicate that the volume fraction of unreacted particles drops from 29.7% to 4.0%, whereas porosity in AAFS paste goes up from 4.1% to 15.4% at up to 800 ºC. The average hardness and elastic modulus are in the ranges of 0.6-14.5 GPa and 27.0-104.2 GPa, respectively. Based on the obtained experimental results, the microstructure-micromechanical property relations and inherent damage mechanisms were then discussed in depth from a multiscale viewpoint.

Keywords: Geopolymer; Microstructure; Micromechanical properties; Damage mechanism; Nanoindentation

1. Introduction

Alkali-activated materials (AAM) have been considered as a promising alternative to ordinary Portland cement because of their superior mechanical performance, significant reduction in CO_2 emissions, consumption of industrial wastes and application of recycled materials [1-7]. Compared to the commonly used types of AAM such as alkali-activated fly ash (AAF), alkali-activated slag (AAS) and alkali-activated metakaolin (AAMK), alkali-activated fly ash-slag (AAFS) is an attractive type of AAM in blend precursor system, which combines the advantages of AAF and AAS to achieve excellent engineering properties and durability at ambient temperature curing [8-11]. Therefore, the focuses have been placed on the behaviour of AAFS in different scenarios to explore its potential

* Corresponding authors. E-mail address: mingzhong.zhang@ucl.ac.uk (M. Zhang)

applications. In particular, high-temperature exposure can be one of the most crucial factors that determines the suitability of AAFS as fire-resistant and thermal energy storage materials [12-14]. Thus, it is vital to carry out a thorough investigation into the high-temperature performance of AAFS.

Many studies have explored different mechanical and thermal properties of AAFS at elevated temperatures and the main damage mechanisms can be summarised with three different temperature levels: a) 20-200 ºC: further geopolymerisation and pore pressure build-up [15-17], b) 200-600 ºC: thermal gradient and phase decomposition [16, 18], and c) 600-800 ºC: recrystallisation and viscous sintering [16, 17, 19-21]. Heating beyond 800 ºC can lead to the loss of structural integrity in the matrix. In terms of mechanical properties, the increase of temperature at up to 400 ºC would lead to a compressive strength gain by around 20-78%, depending on the fly ash/slag ratio [16, 22, 23]. After exceeding 400-600 ºC, a significant drop in retention strength by up to 140% was found in AAFS, followed by a slight rise in strength at 800 ºC due to viscous sintering [14, 16, 24]. As for thermal properties, the experimental study on thermal stability of AAFS paste indicated that the main mass loss occurred before reaching 400 ºC [16, 17]. A major thermal contraction was observed in AAFS paste at around 680 ºC due to the collapse of nanostructure induced by high temperature exposure [16]. Then, a thermal expansion could be found in AAFS matrix, ascribed to the formation of large cracks at around 800 ºC.

To gain insights into the changes in mechanical and thermal properties, the microstructural evolution of AAFS at both ambient and elevated temperatures has recently been explored from a multiscale point of view in a few studies [17, 25]. The change of nanostructures in terms of compositions of different reaction products (i.e., N-A-S-H, C-A-S-H and N-C-A-S-H gels) in AAFS paste was examined, indicating the decomposition of C-A-S-H gels, formation of N-A-S-H gels and phase transformation between amorphous and crystalline phases from 20 to 800 ºC [17, 25]. In addition, the morphological change within AAFS paste was also studied, showing the appearance of large cracks, cavities and flaws in a porous structure with a porosity of around 24% at 800 ºC [25, 26]. Although some of microstructural features in AAFS have been characterised before and after heating, a comprehensive understanding of the evolution of micromorphology and gel compositions, as well as the relationships between microstructure and mechanical performance in AAFS at elevated temperatures is still lacking.

Apart from microstructural characteristics, the micromechanical properties that contribute to the macroscopic mechanical performance of AAFS paste were rarely explored. The existing studies are mainly focused on the micromechanical properties of AAFS paste at ambient temperature. At the paste level, the local elastic modulus and hardness were tested on different solid phases, including unreacted particles and reaction products. Regarding unreacted particles, the unreacted fly ash and slag were found to have an elastic modulus of 30-140 GPa and 46-70 GPa, respectively [26-29]. The

elastic modulus of reaction products in AAFS paste was also measured, including N-A-S-H gels (4-20 GPa), C-A-S-H gels (12-47 GPa) and N-C-A-S-H gels (15.6-23.9 GPa) [27-32].The change in chemical compositions and internal structures would affect the evolution of elastic modulus in AAFS paste in terms of local chemical environment and heterogeneity of the structure. However, AAFS paste could experience drastic physic-chemical changes induced by elevated temperatures, whereas no work has attempted to explore the micromechanical properties of AAFS paste after exposure to high temperatures and link them with microstructural characteristics.

To fill in the gap of knowledge, this study conducts a systematic investigation into the microstructure and micromechanical properties of AAFS paste subjected to elevated temperatures (20, 105, 200, 400, 600 and 800 ºC), and aims to provide new insights into the relationships between them as well as their contributions to high-temperature performance of AAFS. Regarding microstructural features, the temperature-dependent micromorphology of AAFS paste was characterised using backscattered scanning electron microscopy-energy dispersive spectroscopy (BSEM-EDS), while the micromechanical properties in terms of local elastic modulus and hardness of AAFS paste were examined using atomic force microscopy (AFM) and nanoindentation. Based on the obtained experimental results and the authors' previous studies [16, 25], the microstructure-micro/macro-mechanical property relations in AAFS paste were explored in depth for the first time to gain insights into the underlying damage mechanisms of AAFS at elevated temperatures.

2. Experimental program

2.1 Raw materials

Low-calcium (equivalent to ASTM Class F) fly ash and ground granulated blast-furnace slag (GGBS) were used as precursors in this study, the chemical compositions and particle size distribution of which are presented in **Table 1** and **Fig. 1**, respectively. Based on the previous research [33], 10 M sodium hydroxide (SH) and commercial sodium silicate (SS) were used as alkaline activators. The 10 M SH was prepared by incorporating 400 g NaOH pellets (analytical level of 99 wt.%) with 1 L water. It was then stored for 24 h to release heat and cool down to ambient temperature before mixing. The modulus (molar ratio of SiO_2/Na_2O) of SS solution (Na_2O: 8.5 wt.%, SiO_2:27.0 wt.%, H_2O: 64.5 wt.%) was set as 2.0. To ensure the workability of the AAFS mixtures, the polycarboxylate-based superplasticiser (SP, Sika®ViscoFlow®2000) was used as the admixture [32-35].

Table 1 Chemical compositions (wt.%) of fly ash and slag.

Oxide	SiO_2	Al_2O_3	Fe_2O_3	CaO	K_2O	MgO	TiO_2	Na_2O	SO_3	P_2O_5	MnO
Fly ash	47.51	28.68	7.28	8.02	1.52	1.46	1.00	1.05	0.68	2.35	-
Slag	32.61	16.90	0.33	39.61	0.30	7.28	0.55	0.38	-	0.03	0.26

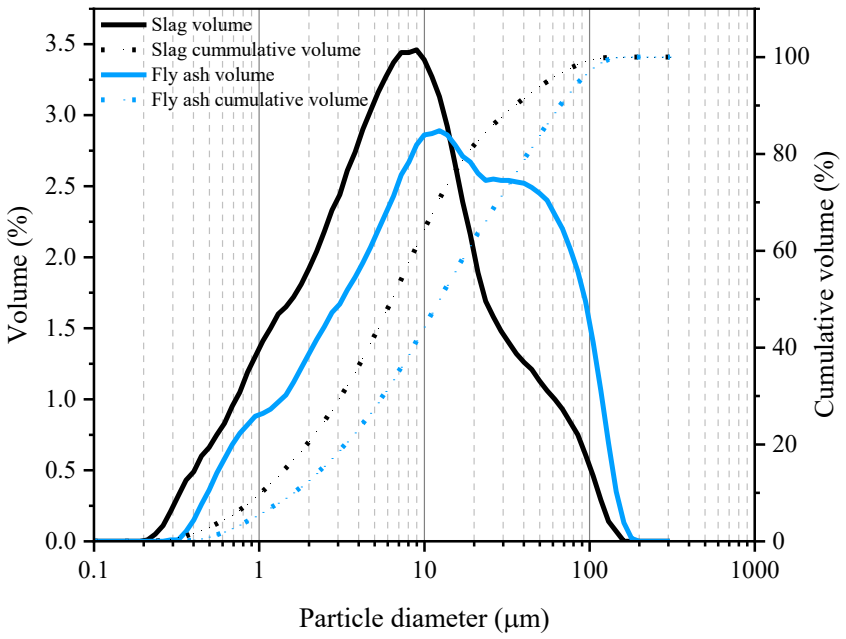

Fig. 1. Particle size distribution of fly ash and slag.

2.2 Mix proportion

The mix proportion of AAFS paste adopted here was determined based on a previous study [33], which can meet the criteria for engineering applications in terms of fresh properties (e.g., workability and setting time) and mechanical performance (i.e., 28-d compressive strength should exceed 35 MPa according to ACI M318-05 [36]). The relevant proportions of different components were set as follows: fly ash/slag ratio = 4, alkaline activator-to-precursor ratio (AL/P) = 0.4, SS/SH = 0.2, superplasticiser-to-precursor ratio (SP/P) = 0.01. The mixture quantity is given in **Table 2**.

Table 2 Mix proportion (kg/m^3) of AAFS.

	Fly ash	Slag	SH	SS	SPs
Mixture quantity	320	80	53	107	4

2.3 Sample preparation

To prepare the fresh AAFS paste, firstly, the precursors (fly ash and slag) were dry mixed for 3 min. Afterwards, the liquid solutions including SH, SS and SPs were added into the mixture and continued mixing for another 3 min. The fresh AAFS paste was cast into two different moulds, i.e., plastic tube moulds (⌀15 × 100 mm) and plastic cubic moulds (40 × 40 × 40 mm) after mixing, and placed on a vibrating machine for 2 min. The specimens were then sealed with plastic film and cured in a standard curing room (20 ± 2 ºC, 95% relative humidity) for 28 d before testing. **Fig. 2** illustrates the preparation of cylinder and crushed specimens. Six cylindrical samples were prepared from each tube for nanoindentation test, whereas the crushed specimens from the cone of the cube were used for BSEM-EDS test.

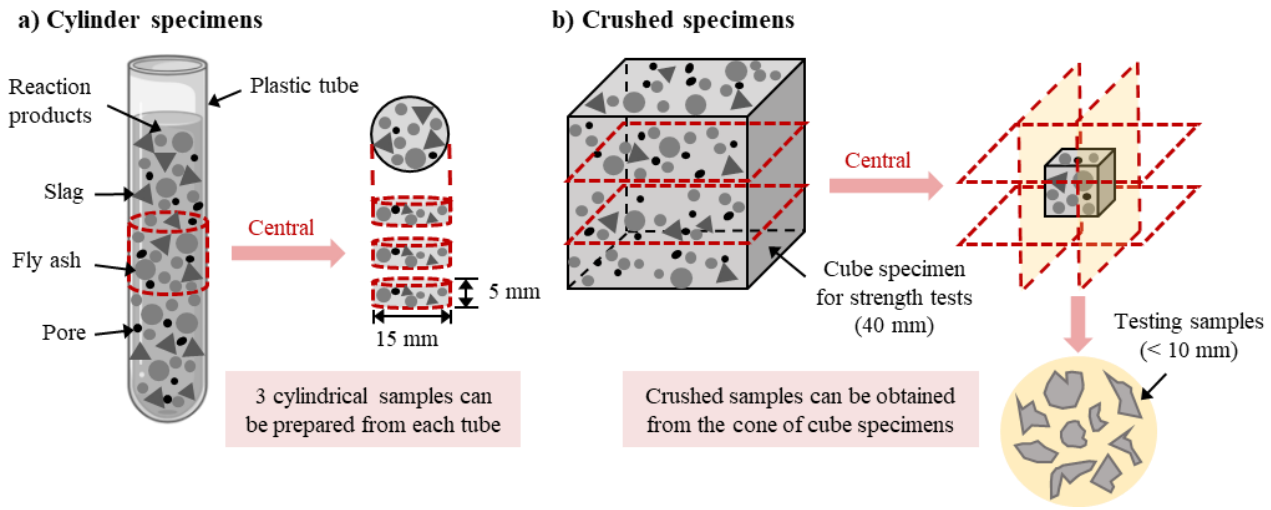

Fig. 2. Schematic illustration of (a) cylinder and (b) crushed specimen preparation.

2.4 Heating methods

In this study, the heating rate was set as 10 °C/min to obtain the target temperatures of 105, 200, 400, 600 and 800 °C [14, 16, 37, 38]. The samples were placed in an electrical furnace with a computed heating curve. When the target temperature was reached, it was held in the furnace for 120 min to ensure uniform distributed temperatures within the specimen, and thus a thermal equilibrium state could be achieved [21]. Afterwards, the specimen was naturally cooled down to room temperature.

2.5 Testing methods

2.5.1 Backscattered electron microscopy-energy dispersive spectrometry (BSEM-EDS)

A field emission scanning electron microscope was used to characterise the microstructure and morphology changes of AAFS specimens. The working distance was set as 10 mm with the acceleration voltage of 20 kV and the spot size of 6 nm. The pixel size for the images was 270 nm at a magnification spanning from 30× to 4000×. Furthermore, the EDS analysis was conducted under the conditions: beam energy of 15 keV, probe current of 600 pA, and beam spot size of about 450 nm. The working distance was 8.5 mm with a take-off angle of 35º. The counting rate was set as 50000 counts per analysis with dead times of 30% and acquisition time of 50 s.

2.5.2 Nanoindentation

The nanoindentation test was conducted to examine the micromechanical properties of AAFS paste in terms of local elastic modulus and hardness [32]. Herein, the nanoindentation instrument with a Berkovich indenter tip (BRUKER, Hysitron TI 950, Germany) was used, with the load and displacement resolution of 1 nN and 0.04 nm, respectively. The loading curve of nanoindentation test includes three segments: 1) constant loading rate of 400 μN/s until the maximum load of 2 mN was achieved, 2) holding time of 2 s at the maximum load, and 3) unloading rate of 400 μN/s. The classical nanoindentation modes were applied in this study. 20 indentation tests were performed at different locations (i.e., unreacted particles and reaction products) of AAFS paste specimens in the classical mode. **Fig. 3** shows the examples of indentation locations in the AAFS paste at 20, 400 and 800 °C.

2.5.3 Atomic force microscopy (AFM)

The atomic force microscopy (AFM) test was carried out to measure the surface topography of the polished AAFS paste specimens using the AFM instrument (Bruker, Dimension ICON, USA).

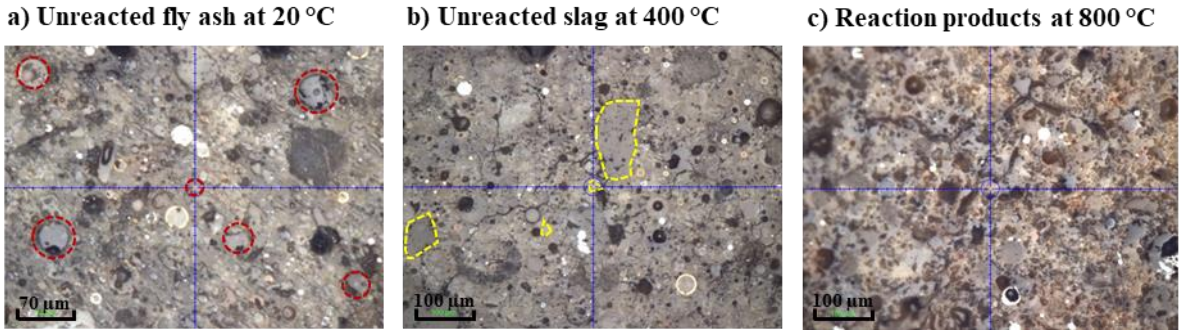

Fig. 3. Examples of indentation locations in AAFS paste at various exposure temperatures.

3. Results and discussion

3.1. Micromorphology

With the increase of exposure temperature, AAFS paste experiences physical and chemical changes that trigger the change of microstructural features in different phases. **Fig. 4** shows the evolution of micromorphology in AAFS paste from 20 to 800 °C based on BSEM images. At 20 °C, the dispersion of unreacted fly ash and slag can be clearly observed in light grey colour with spherical and angular shapes, respectively. As the temperature rises to 105 °C, there is no noticeable micromorphology change within the AAFS matrix. The microcracks tend to propagate and further develop along the "weak region" at the edge of unreacted fly ash and slag, i.e., interfacial transition zone between different solid phases in AAFS paste [17]. At 200 °C, the unreacted fly ash and slag particles become more difficult to be identified, which can be attributed to the dissolution of raw materials and further geopolymerisation within the specimen [39, 40]. Following by the further development of cracks in AAFS paste at 400 °C, there exists a significant change in micromorphology with phase transformation in the specimen after 600 °C exposure. At this temperature level, unreacted particles can seldomly be observed, whereas microcracks turn into large cracks and cavities. After 800 °C, a porous internal structure can be observed in AAFS matrix. This can be ascribed to viscous sintering associated with interparticle bonding and gel densification, as well as phase transformation and crystallisation from amorphous to new crystalline phases, including nepheline and gehlenite [16, 19, 41, 42]. Due to the significant mineralogical changes in AAFS paste between 600 and 800 °C, the resulting alterations in sample morphology can be found in **Figs. 4** and **5**.

3.2. Phase assemblage

To investigate the microstructural evolution of AAFS paste from 20 to 800 °C, 12-15 images were captured from the corresponding samples for each temperature level. The compositions of different phases in AAFS paste at various temperature levels were determined based on the quantitative analysis of greyscale diagrams of BSEM images where unreacted particles, reaction products and

pores/cracks appear in light grey, dark grey and black, respectively, as seen in **Fig. 4** [43-45]. The image processing was conducted following the approach described in previous work [16], where thresholds for each phase were determined based on the intersection points of different greyscale curves. This method ensured consistency across all analysed images by applying the same thresholds during image segmentation [16]. However, it is important to note that the captured BSEM images are 1536×1094 pixels with a pixel size of 270 nm (192 dots per inch). This means that any features related to unreacted particles, reaction products, and pores with a diameter smaller than 270 nm would not be detected, which may consequently affect the accuracy of phase quantification, particularly in regions where different phases exhibit similar grey values.

After image segmentation, all three phases are colour-coded separately in blue (unreacted particles), yellow (reaction products) and red (pores and cracks). **Fig. 5** demonstrates the phase assemblage of AAFS with corresponding visualisation based on the processed BSEM images at each temperature level from 20 to 800 °C. As mentioned before, unreacted particles with the highest volume fraction of 29.7% can be found in the paste specimen at 20 °C, followed by a gradual decline to 18.8% at up to 400 °C and a sudden drop by approximately 36.3% when reaching 600 °C. Due to the continuous high temperature exposure and sintering effect, the unreacted particles only takes up 4.01% of the total volume at 800 °C, as observed from the segmented image with almost negligible blue regions [46-48]. Regarding reaction products, a continuous increase from around 66.2% to 82.7% happens when the temperature rises from 20 to 600 °C, while there is a slight decline of the volume fraction from 82.7% to 80.6% after 800 °C is reached, as a result of the drastic phase transformation at this stage of heating [20, 24, 49, 50]. Regarding pores and cracks, the volume fraction is relatively stable at around 4-5% in the paste until up to 600 °C exposure. Afterwards, there is a comparative increase from 5.1% to 9.3% and 15.4%, respectively, when the temperature reaches 600 and 800 °C.

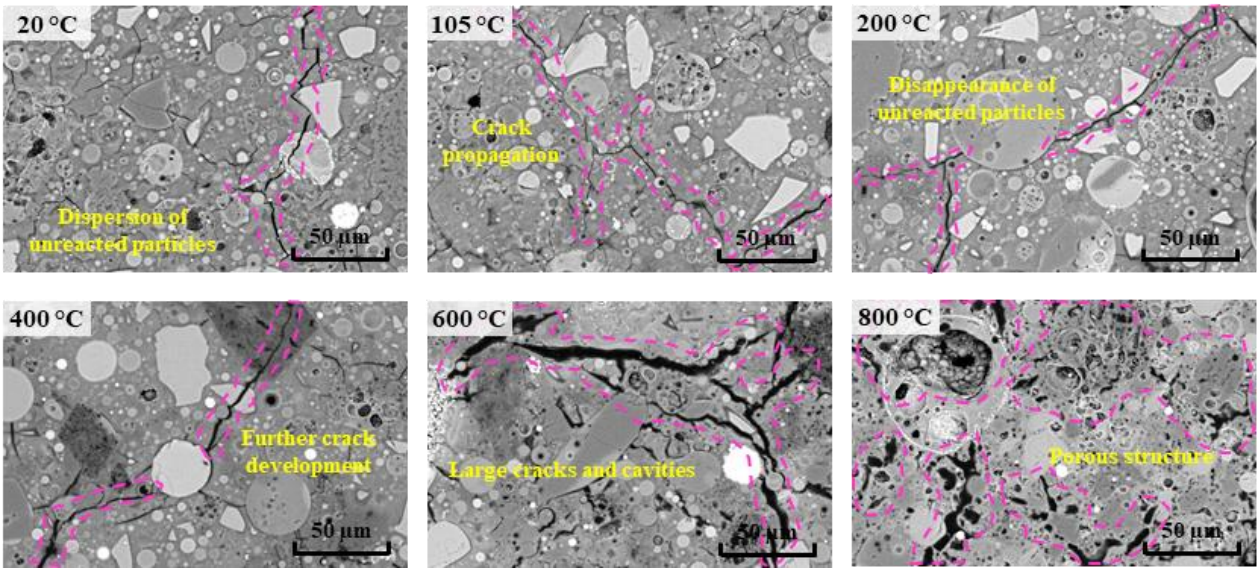

Fig. 4. Evolution of micromorphology in AAFS paste at various exposure temperatures.

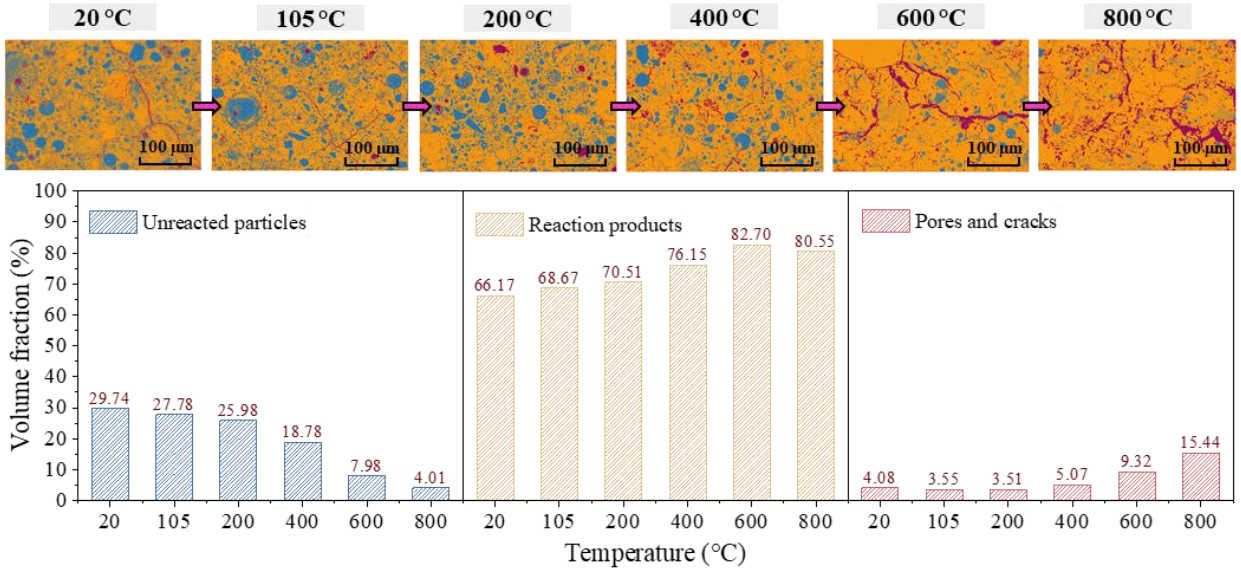

Fig. 5. Phase assemblage of AAFS paste at elevated temperatures based on BSEM images.

3.3. Gel compositions

To further investigate the gel compositions in reaction products of AAFS paste, the local element maps regarding Si, Al, Ca and Na in the specimen at elevated temperatures are displayed in **Fig. 6**, indicating that part of Si and Ca concentrate at the region of unreacted fly ash and slag particles. Whereas, the rest of the mentioned elements are relatively evenly distributed in the reaction products, consisting of N-A-S-H gels (i.e., SiO_4 and AlO_4 tetrahedra in a highly cross-linked structure with shared O atoms [51]), C-A-S-H gels (i.e., silicate chains inter-linked by layers of CaO [52-54]), and N-C-A-S-H (i.e., modification of N-A-S-H gels by partially replacing Na^+ with free Ca^{2+} to form the hybrid structure [26, 55, 56]).

Fig. 7 illustrates the compositional ternary diagram of CaO-SiO_2-Al_2O_3 in AAFS matrix at elevated temperatures from 20 to 800 °C based on the EDS point scanning results focusing on the reaction products. As per the existing studies on the compositional ranges of different types of reaction products [26, 56-59], the majority of the points are within the region of C-A-S-H and high Ca C-(N)-A-S-H gels in reaction products from 20 to 200 °C. As the temperature rises to 400 and 600 °C, the spots tend to shift towards right and concentrate at the region with relatively less Ca involvement. After 800 °C exposure, more spots appear in the low-calcium region, which are categorised as N-A-S-H and N-C-A-S-H gels.

To quantitatively analyse the gel compositions, the statistical distribution of Al/Si and Ca/Si ratios in AAFS at elevated temperatures is demonstrated in **Fig. 8**. As seen in **Fig. 8(a)**, the average Al/Si ratio stays around 0.36-0.46 in the paste after heating at up to 400 °C, which can be recognised as Si-rich N-A-S-H gels (i.e., the Al/Si ratio of Si-rich N-A-S-H gels is around 0.5 [60]). From 400 to 800 °C, there is a noticeable increase of the Al/Si ratio from approximately 0.40 to 0.79, implying an increase of Al-rich N-A-S-H gels in the reaction products of AAFS paste after 400 °C exposure. This

is consistent with the nuclear magnetic resonance (NMR) results from the previous research that the silicon tetrahedra with a $Q^4(3Al)$ structure referring to highly cross-linked Al-rich N-A-S-H gels exhibits a significant increase of volume fraction from 21.6% to 41.3% at 400-800 °C [25]. In terms of Ca/Si ratio in the paste, a rise in the average ratio from around 0.64 to 0.81 at 20-105 °C occurs, attributing to the continuous dissolution of slag and further geopolymerisation triggered by temperature exposure. As the temperature goes up from 200 to 800 °C, there is an overall trend of decline in Ca/Si ratio of the specimen from 0.68 to 0.55 with a slight fluctuation at 400-600 °C (see **Fig. 8(b)**). This can be ascribed to the release of free Ca^{2+}, decomposition of C-A-S-H gels and potential phase transformation from C-A-S-H (Ca/Si ratio of around 0.67-3) to N-(C)-A-S-H (Ca/Si ratio of around 0.14-0.33) and C-(N)-A-S-H (Ca/Si ratio of around 0.45-10) gels at up to 800 °C [55, 56, 60-64].

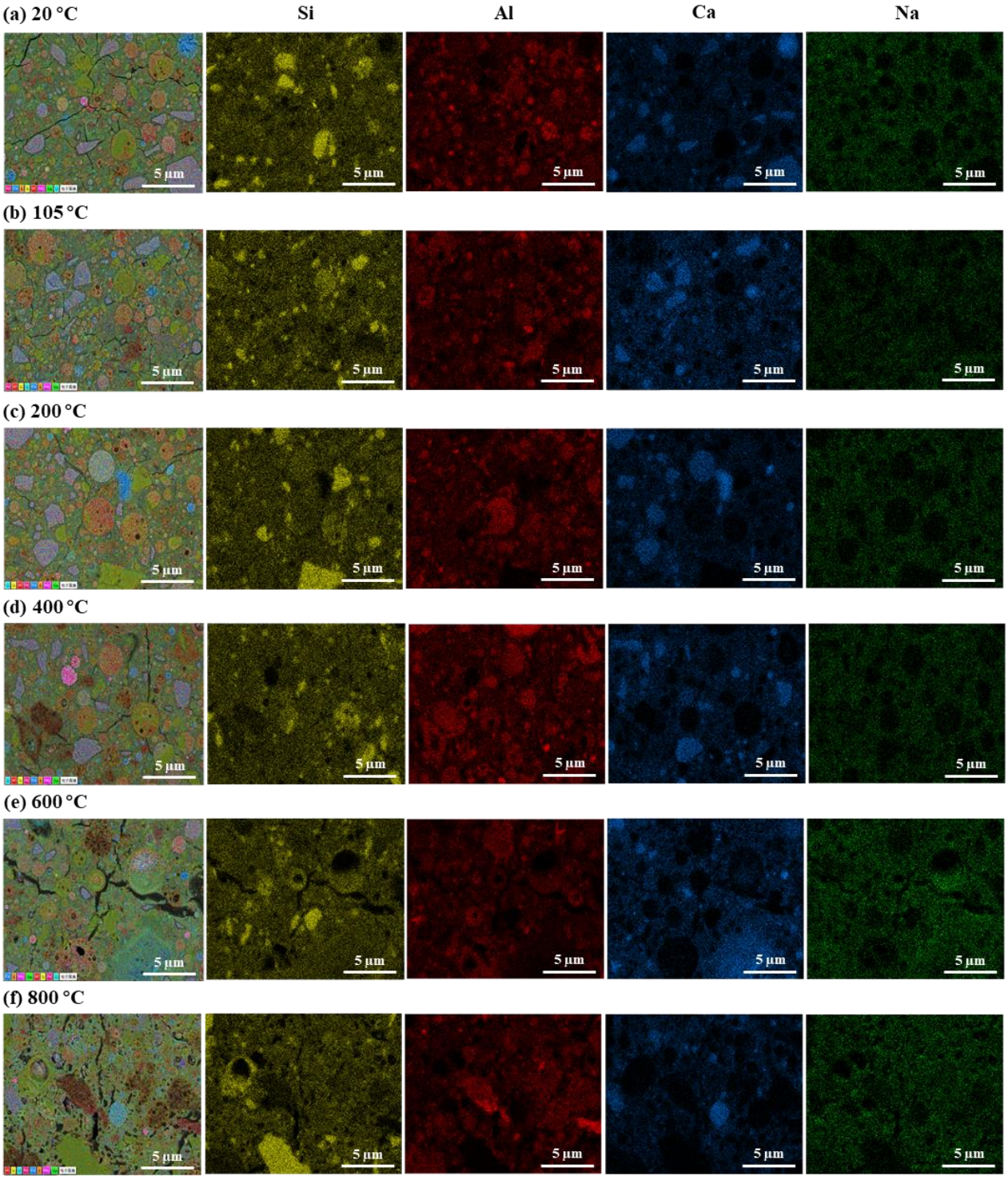

Fig. 6. EDS analysis of AAFS paste at elevated temperatures.

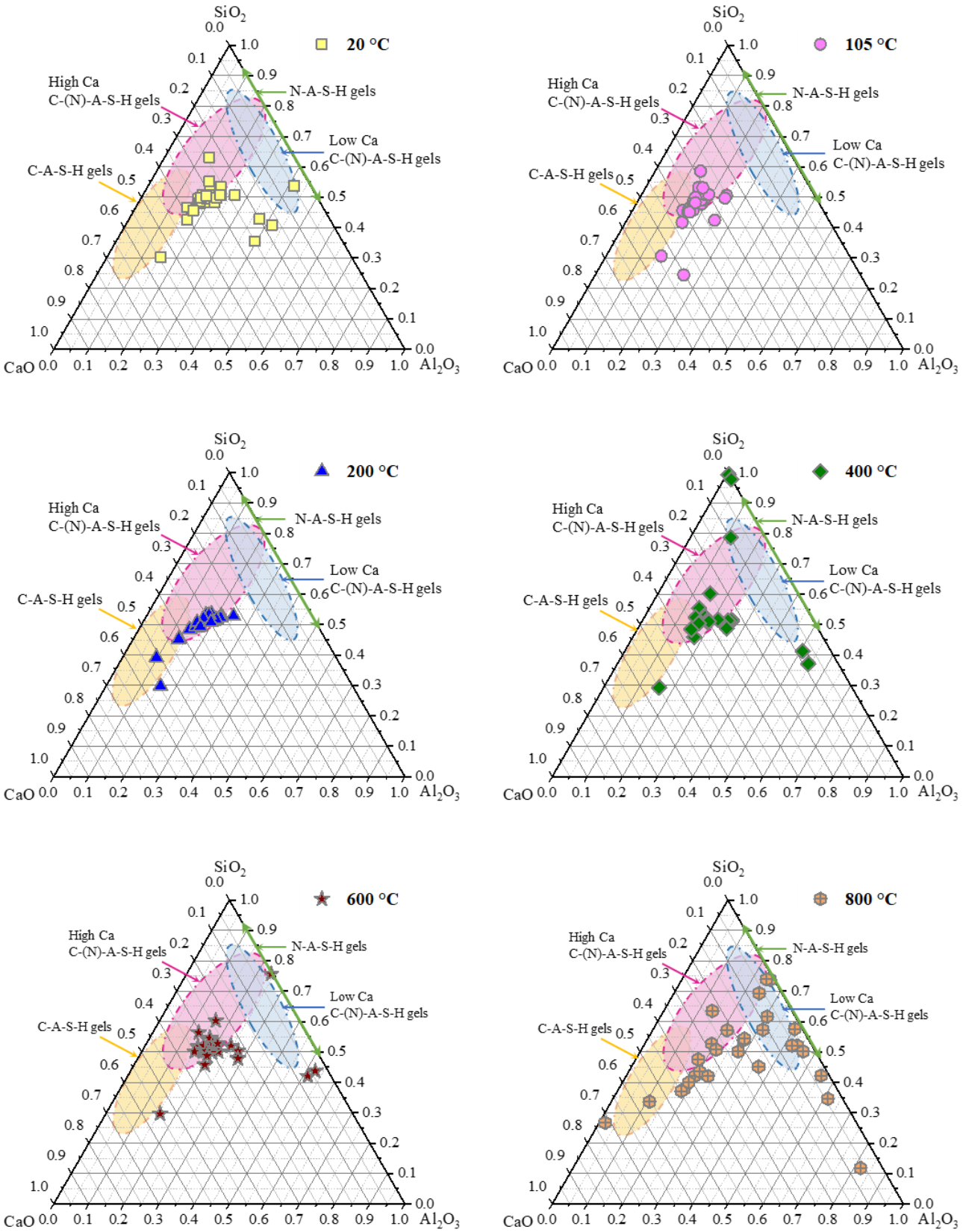

Fig. 7. Compositional ternary diagram of CaO-SiO_2-Al_2O_3 in AAFS paste at elevated temperatures (Note: compositional ranges of binder gels adapted from [26, 56-59]).

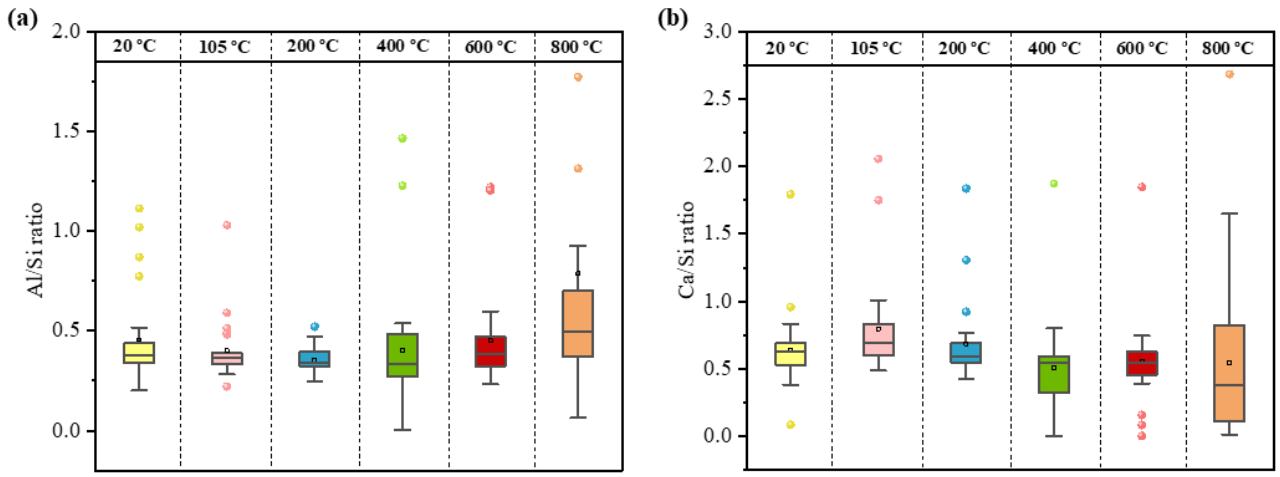

Fig. 8. Statistical distribution of (a) Al/Si and (b) Ca/Si ratios in AAFS paste at elevated temperatures based on the EDS analysis.

3.4. Surface roughness

To examine the micromechanical properties, the surface roughness was measured using AFM to evaluate the surface conditions of specimens. **Fig. 9** displays the variations in surface topography of AAFS paste at elevated temperatures in both 2D and 3D AFM images. A relatively smooth texture is shown in the specimens after exposed to 20 to 600 °C, whereas an irregular porous surface can be observed in the specimen at 800 °C. This is consistent with the rough surface found in the BSEM image of AAFS paste after 800 °C exposure, which contains cavities and flaws in a porous structure. To characterise the surface roughness, two different amplitude parameters are used to quantify the topography of samples, including the average roughness R_a and the root mean square R_q [65]. **Table 3** summarises the roughness number of the specimens obtained from the AFM results. It is indicated that R_a ranges from 13.0 to 102 nm with a mean value of 44.3 nm, while R_q ranges from 18.5 to 132 nm with a mean value of 59.3 nm. These roughness values indicate the quality of the sample's surface preparation, which is crucial for accurate nanoindentation analysis, as indentations must occur on a flat surface [66]. Based on the surface roughness criteria concluded in the previous studies, the R_q values should be 3-5 times less than the indentation depth [66, 67]. Given that the average indentation depth is approximately 180 nm, the maximum permissible R_q value is around 900 nm. The obtained R_q values are well below this threshold, which suggests the sample surfaces have been ground and polished effectively, thereby minimising the influence of surface roughness on the indentation results.

Table 3. Summary of surface roughness number (nm) in AAFS paste at elevated temperatures.

Temperature	20 °C		105 °C		200 °C		400 °C		600 °C		800 °C	
Roughness	R_a	R_q	R_a	R_q	R_a	R_q	R_a	R_q	R_a	R_q	R_a	R_q
Capture1	43	55.2	101	132	17.5	22.6	13.0	23.1	32.7	42.6	21.1	29.2
Capture2	62	84.4	91.1	116	55.4	67.8	13.8	18.5	36.7	46.6	23.4	33.1
Capture3	61.6	94.9	102	130	52.9	75.7	23.4	32.6	23.4	29.3	22.9	34.5

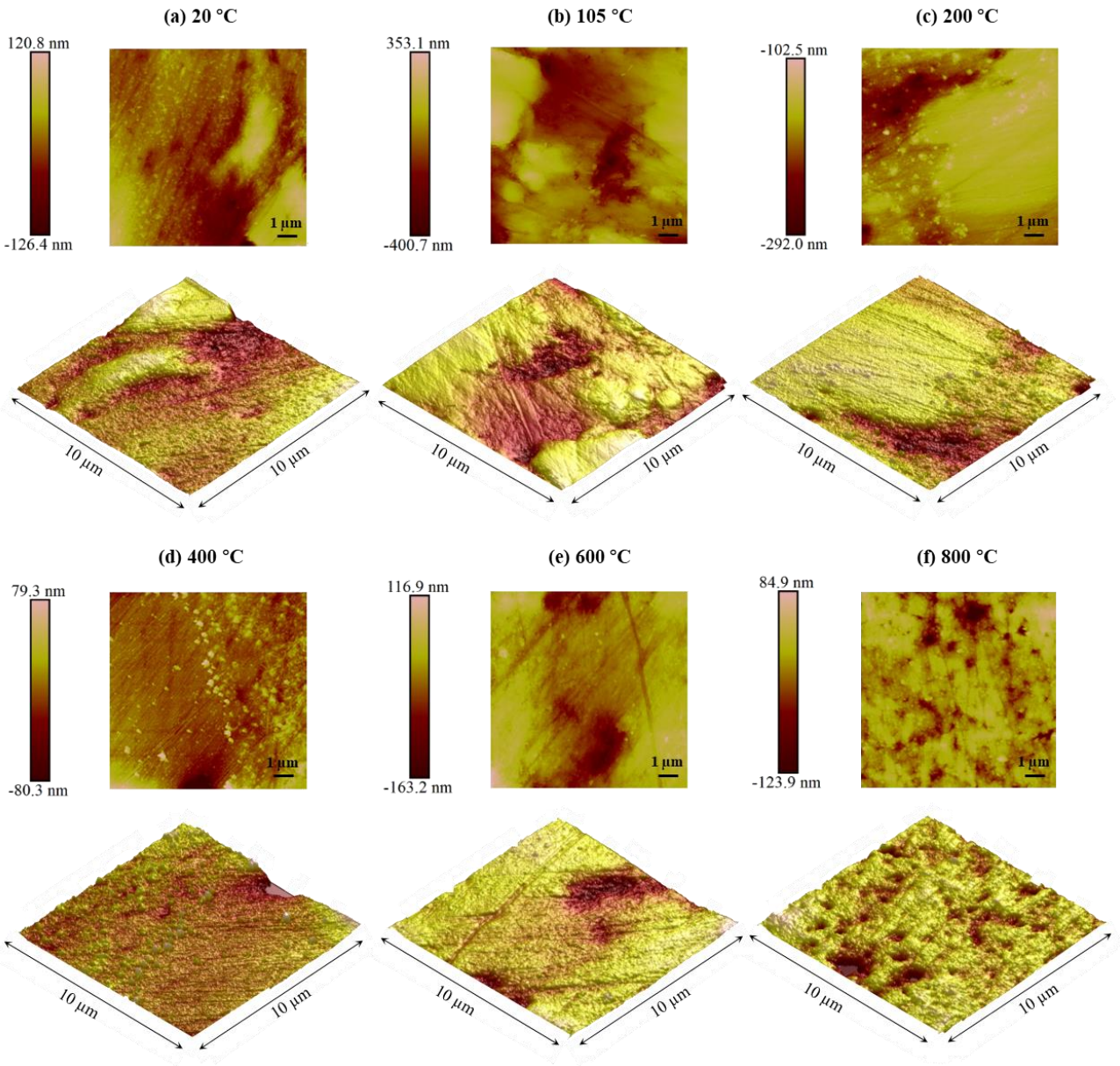

Fig. 9. Surface topography of polished AAFS paste before and after high temperature exposure.

3.5. Hardness

Nanoindentation test was performed on the polished specimens to determine the micromechanical properties of different solid phases in AAFS paste at elevated temperatures. After experiencing the process of loading, constant holding and unloading, the indentation load and depth were tracked to determine the indentation modulus, hardness and elastic modulus of samples [26, 68]. The load-displacement curves of AAFS pastes are shown in **Fig. 10(a)**. The average indentation depth in the specimen is around 160 nm, suggesting that the prepared sample is comparatively smooth to minimise the effect of surface topography on the indentation results in terms of the aforementioned mean roughness numbers of 44.3 nm and 59.3 nm for R_a and R_q, respectively. According to the curves, unreacted slag particles exhibit the lowest indentation depth of around 80-90 nm, while unreacted fly ash particles have a wider range varying from around 80 to 200 nm. The indentation depth of reaction products ranges from approximately 175 to 280 nm. **Fig. 10(b)** demonstrates the relationship between

elastic modulus and hardness of AAFS paste subjected to different temperatures. The hardness of reaction products was found to be in the ranges of 0.59-0.73 GPa for N-A-S-H gels and 0.3-2.5 GPa for C-A-S-H gels, while the hardness of unreacted particles was typically reported to be around 6 GPa [26, 27, 31, 69, 70]. In this study, the overall hardness of AAFS paste at 20-800 °C is in the range of 0.6-14.5 GPa, which distinctly shows the micromechanical responses of different solid phases in the paste. Furthermore, the tendency of a higher hardness can also be denoted in AAFS paste when the temperature rises from 20 to 800 °C.

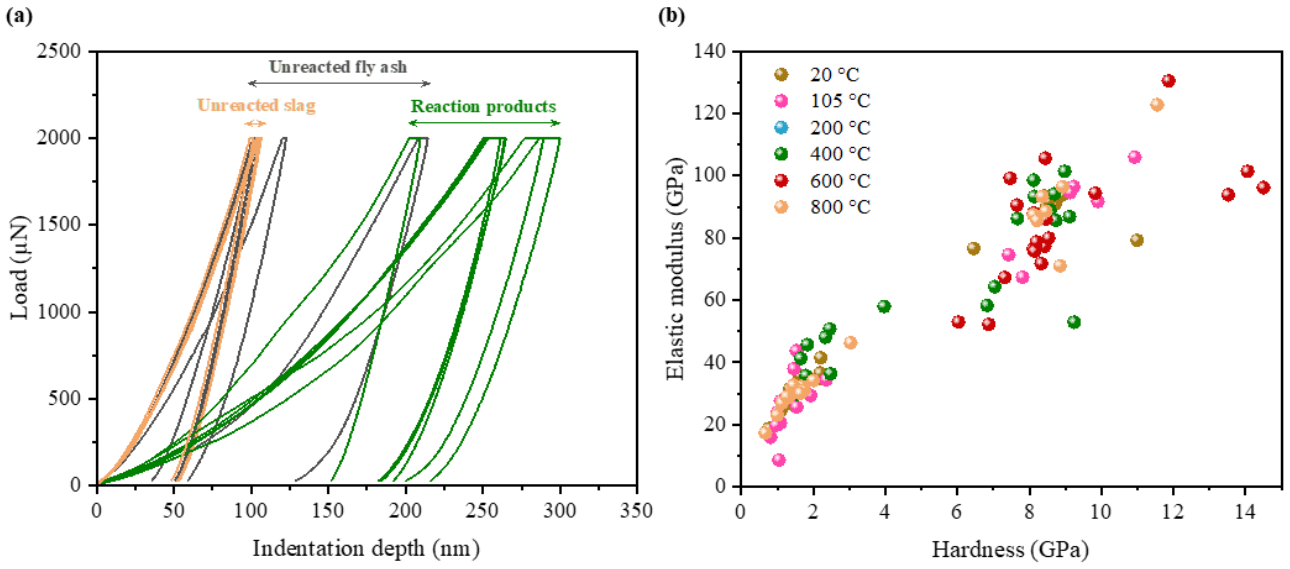

Fig. 10. (a) Load-displacement curves of different solid phases (i.e., unreacted fly ash, unreacted slag and reaction products) in AAFS paste at 20℃, and (b) elastic modulus and hardness of AAFS paste at elevated temperatures.

3.6. Elastic modulus

Fig. 11 presents the elastic modulus of unreacted particles and reaction products in AAFS paste at elevated temperatures. As per the previous studies, the elastic modulus of unreacted fly ash was dependent on the mineral features, ranging from 30 to 140 GPa , while the elastic modulus of unreacted slag was in the range of approximately 46-70 GPa [27, 60]. As seen in **Fig. 11(a)**, the average elastic modulus of unreacted fly ash and slag particles at 20℃ is 85.1 GPa and 92.3 GPa, respectively. The obtained elastic modulus of unreacted fly ash is within the range of 30-140 GPa, whereas that of unreacted slag is relatively higher than 70 GPa reported in the previous literature. With the rising exposure temperature, the average elastic modulus of unreacted fly ash particles varies from around 78.4 to 90.0 GPa, whereas that of unreacted slag particles ranges from 88.6 to 104.2 GPa at up to 800℃. In general, unreacted fly ash and slag particles are expected to be thermally stable, given that they are produced through processes occurring at temperatures significantly exceeding 1000 ºC . However, the discrepancies in the elastic modulus of unreacted particles can be associated with different factors. Regarding fly ash, the dissolution rate can be dependent on the heterogeneity

of particles, as they contain both inert crystal phases and reactive amorphous phases with a random distribution [43, 71]. Unlike fly ash with a spherical shape, slag particles have a more irregular shape with relatively higher angularity, which also causes inhomogeneous dissolution of unreacted particles and therefore the variation of elastic modulus [26, 31]. Moreover, the interaction between fly ash and slag particles (i.e., modification of nanostructure and chemical compositions) can also make a pronounced effect on the dissolution process and surrounding reaction products, leading to the differences of their elastic moduli [43, 57, 72]. It should be noted that the micromechanical responses of unreacted particles were obtained from limited data using classic indentation method. In the classic indentation method, indentation tests are performed at various locations on the sample surface, with these locations selected based on surface observation alone. This approach may present challenges in accurately identifying interfacial transition zones between different phases, e.g., unreacted particles and reaction products. Future research could benefit from the grid-indentation technique, which systematically covers an entire region with programmed indentation locations, rather than relying on manually selected points and thus it may enhance the precision and reliability of phase characterisation in the material.

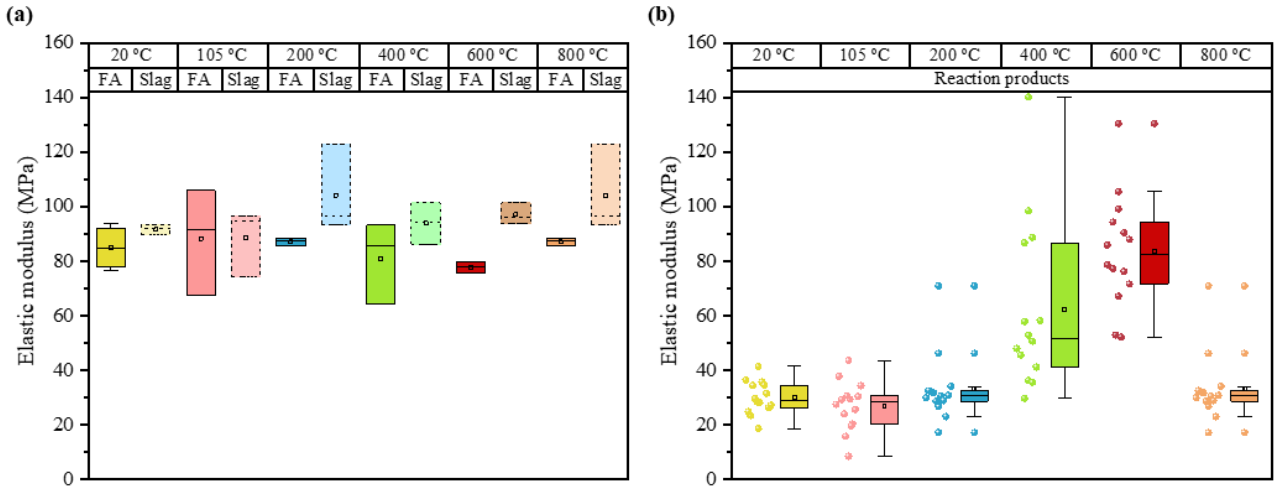

Fig. 11. Statistical distribution of elastic modulus of (a) unreacted particles and (b) reaction products in AAFS paste at elevated temperature.

Regarding reaction products shown in **Fig. 11(b)**, the average elastic modulus of reaction products in AAFS paste tends to be relatively stable at around 27.0-33.9 GPa from 20 to 200 ºC. This suggests the stability of reaction products without significant phase decomposition and transformation at this stage, which is in good agreement with the previous research that the dominant damage mechanisms are further geopolymerisation and pore pressure build-up at up to 200 ºC [16]. Afterwards, there is a significant increase in the average elastic modulus by 50.3-84.2 GPa from 200 to 600 ºC, followed by a sudden drop of 150.6% to 33.6 GPa at 800 ºC. It can be found that the phase transformation among different binder gels takes place. At 20 ºC, the elastic modulus of N-A-S-H and C-A-S-H gels was found to be about 4-20 GPa and 12-47 GPa, respectively [27-31]. Whereas, the hybrid N-C-A-

S-H gels have an elastic modulus of 15.6-23.9 GPa [32]. Therefore, the significant decline of average elastic modulus from 84.2 to 33.6 GPa at 600-800 ºC can be ascribed to the decomposition of C-A-S-H gels and formation of new N-A-S-H gels, which is also notified from the SEM-EDS results. As the classic nanoindentation was used to characterise the micromechanical properties of AAFS paste in this study, the future work can be focused on grid nanoindentation to capture detailed features in ITZ, pore and cracks. Overall, the elastic modulus of unreacted fly ash and slag particles is dependent on their mineral features, shape and local reactivity, while the decomposition and transformation of N-A-S-H, C-A-S-H and N-C-A-S-H gels can significantly affect the micromechanical responses of reaction products in AAFS paste. With the increase of temperature, the simultaneous occurrence of decomposition of C-A-S-H gels (decreased by around 11.5%) and formation of N-A-S-H gels (increased by about 15.3%) in AAFS paste from 400 to 600 °C [25, 39, 73, 74], which agrees well with the EDS results showing the shift of spots from high-calcium to low-calcium zone.

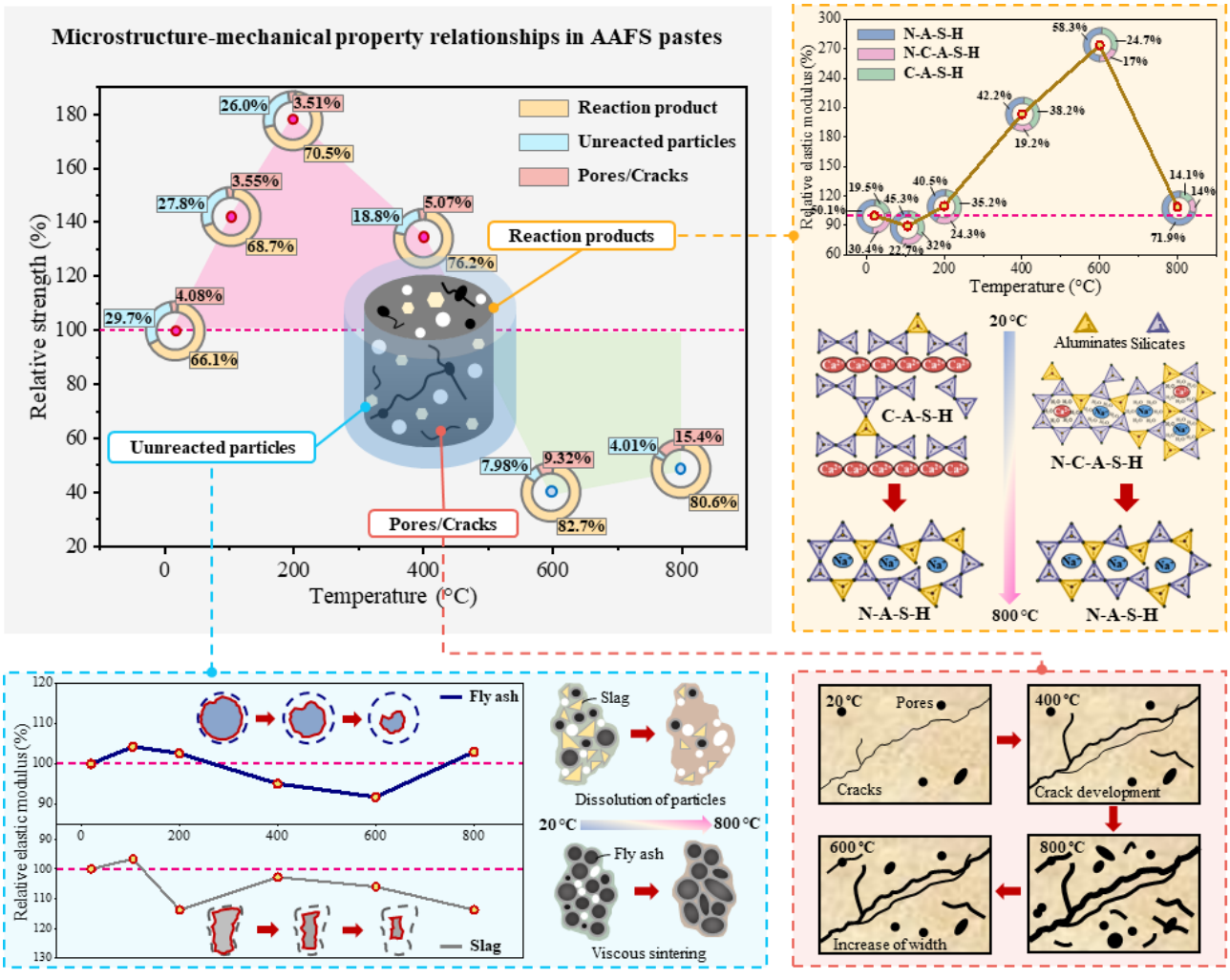

Fig. 12. Schematic illustration of microstructure-micromechanical property relationships in AAFS paste at elevated temperatures.

4. Discussion

Based on the obtained results, the microstructure-micromechanical property relationships in AAFS paste at elevated temperatures are discussed in terms of phase type, volume fraction and micromechanical properties, as illustrated in **Fig. 12**. According to the aforementioned phase assemblage from BSEM images, the evolution of volume fractions of different phases in AAFS paste was analysed. The corresponding relations between microstructure and micromechanical properties will be discussed covering unreacted particles, reaction products, and pores and cracks in the paste.

For unreacted fly ash and slag particles, a significant drop in volume fraction takes place from 20 to 800 ºC, which can be attributed to the dissolution of unreacted particles and ongoing reactions. The raw materials are continuously consumed and thereby form different types of binder gels, depending on the local chemical environment [56, 75-77]. The relative elastic moduli of both fly ash and slag particles exhibit some fluctuations at approximately 90-115%. The surrounding gels tend to be sintered and densified around the remaining particles, leading to less distinct particle boundaries at 800 ºC.

On the other hand, there exists a rise in the volume fractions of reaction products in AAFS paste by up to 14.5% of the total volume from 20 to 800 ºC. During the alkaline activation of fly ash and slag in AAFS paste at 20 °C, different dissolved species can be rearranged and exchanged to form the binder gels [55, 78]. The reaction of aluminium is more rapid and unstable compared to that of silicon, due to a weaker bond in Al-O than Si-O [79]. From 400 to 600 °C, the EDS results report the shift of spots from high-Ca to low-Ca zone, indicating the decomposition of C-A-S-H gels. This is consistent with the previous findings with the simultaneous occurrence of decomposition of C-A-S-H gels (decreased by around 11.5%) and formation of N-A-S-H gels (increased by about 15.3%) in AAFS paste [25, 39, 73, 74]. Furthermore, compared to N-A-S-H gels in AAF paste, the hybrid N-C-A-S-H gels in AAFS paste exhibit a lower stability in maintaining its structure at high temperatures, leading to phase decomposition after around 600 °C heating [14, 17]. After 800 °C, the phase transformation and recrystallisation in AAFS paste happens [16, 17, 80]. The sudden drop of relative elastic modulus of reaction products by around 270% from 600 to 800 °C (**Fig. 12**) indicates the transformation and rearrangement of different phases at this stage. The phase composition of various binder gels in AAFS paste undergoes a notable transformation after exposure to 800 °C. Specifically, the volume fraction of N-A-S-H gels increases significantly from approximately 58% to 72%, while that of C-A-S-H gels decreases by about 10%. Given the disparity in the elastic moduli of N-A-S-H (4-20 GPa) and C-A-S-H (12-47 GPa) gels [27, 28, 32], the reduction in the overall elastic moduli of reaction products can be ascribed to the reorganisation of the gel phases [81]. Moreover, the mechanical properties of AAFS paste can be affected by the internal structures and compositions of different binder gels. It was reported that the morphology-structural change of C-A-S-H gels is

influenced by the Al/Si ratio. When increasing the Al/Si ratio, a more foil-like shape can be observed in C-A-S-H gels, which are darker, denser and more compact with lower porosity and permeability [64, 81]. Since the overall phase content of amorphous phases can experience a dramatic drop from around 84.1% to 36.0% of the total weight [25], the recrystallisation can occur in AAFS paste in terms of formation of nepheline (from N-A-S-H gels) and gehlenite (from C-A-S-H gels) [16].

At 20 °C, there exist several pores and microcracks in AAFS paste, which may be caused by the heterogenous distribution of chemical components and the variability in pore sizes and morphologies within the matrix [26, 62, 82]. Also, both the chemical shrinkage happened during the reaction process inside the specimen and drying shrinkage with loss of moisture through surfaces contribute to the overall shrinkage that leads to the development of cracks in AAFS paste at 20 °C [16, 83]. With the rising temperature, new cracks start to initiate and develop. These cracks are mainly caused by moisture transport as the pore pressure can be trapped in a dense structure with limited internal connectivity in the paste to release the excessive pressure [14, 84-86]. On the other hand, the consumption of unreacted particles and further reaction contribute to the formation of binder gels and filling of pores and voids. Consequently, the overall volume fraction of pores and cracks is influenced by a combined effect. [80, 87]. After 400 °C, the connection between pores and multiple cracks forms an inter-connected network, which can locally release part of the pressure and mitigate the damage induced by pore pressure build-up [80]. Violent deterioration occurs in AAFS paste with the formation of thicker cracks and cavities after 600-800 °C, due to phase transformation and recrystallisation. This leads to a more porous structure with an increase in volume fraction of pores and cracks by approximately 6% which results in the significant strength loss of AAFS paste.

In general, the mechanical performance of AAFS at elevated temperatures is highly associated with different damage mechanisms existed in all three phases, along with changes of their volume fractions and local micromechanical responses. To sum up, from 20 to 400 °C, the primary mechanisms in AAFS paste include moisture transport-induced pressure build-up and further geopolymerisation triggered by elevated temperatures. Between 400 and 600 °C, phase transformation occurs, notably the decomposition of C-A-S-H gels. From 600 to 800 °C, the damage mechanisms are predominantly linked to recrystallisation and viscous sintering.

5. Conclusions

In this paper, a systematic experimental study on the microstructural characteristics and micromechanical properties of AAFS paste at elevated temperatures (20, 105, 200, 400, 600 and 800 ℃) was presented. Based on the obtained results, the main conclusions can be drawn as follows:

- As the temperature increased from 20 to 800 ºC, the volume fraction of unreacted particles in AAFS paste declined from 29.7% to 4.0%, whereas that of pores and cracks went up from 4.1%

to 15.4%. The gradual disappearance of unreacted fly ash and slag was observed, along with the initiation and propagation of cracks, cavities and flaws in a porous structure at up to 800 ºC.

- As for gel compositions, the EDS spots were found to shift from high-calcium to low-calcium region at elevated temperatures, implying the transformation of binder gels from C-A-S-H to N-A-S-H and N-C-A-S-H gels. Especially, a significant rise in the average Al/Si ratio from 0.40 to 0.79 can be observed with the rising exposure temperature from 400 to 800 °C, indicating the formation of Al-rich N-A-S-H gels.
- An increase of the average Ca/Si ratio from 0.64 to 0.81 was found in AAFS paste after 20-105 °C exposure, which can be ascribed to the newly formed C-A-S-H gels via further geopolymerisation. From 200 to 800 °C, the Ca/Si ratio in AAFS paste tended to drop from 0.68 to 0.55, owing to the decomposition of binder gels and phase transformation.
- Regarding micromechanical properties of AAFS paste, the overall hardness ranged from 0.6 GPa to 14.5 GPa at 20-800 °C. The average elastic moduli of unreacted fly ash and slag particles varied between 78.4 GPa and 104.2 GPa at up to 800 °C, depending on their mineral features, shape and local reactivity. The elastic moduli of reaction products in AAFS paste were in the range of 27.0-84.2 GPa before and after high temperature exposure.

Acknowledgements

Guohao Fang gratefully acknowledges the financial support from National Natural Science Foundation of China (Grant No.: 52108232) and Shenzhen Key Laboratory for Low-carbon Construction Material and Technology (Grant No.: ZDSYS20220606100406016). The financial support provided by University College London (UCL) through a Graduate Research Scholarship to the first author is also greatly appreciated. The authors would also like to thank Mr Guanqi Wei, Mr Ruixi Li, Mr Guohong Wang, Miss Rou Gang, Mr Changzhi Jiang and Miss Huiyin Zhong for their help with the experimental work.

References

[1] C.J. Shi, A.F. Jimenez, A. Palomo, New cements for the 21st century: The pursuit of an alternative to Portland cement, Cement Concrete Res 41(7) (2011) 750-763.

[2] J.L. Provis, S.A. Bernal, Geopolymers and related alkali-activated materials, Annu Rev Mater Res 44 (2014) 299-327.

[3] Y. Ma, G. Ye, The shrinkage of alkali activated fly ash, Cement Concrete Res 68 (2015) 75-82.

[4] C. Gunasekara, D.W. Law, S. Setunge, J.G. Sanjayan, Zeta potential, gel formation and compressive strength of low calcium fly ash geopolymers, Constr Build Mater 95 (2015) 592-599.

[5] P. Zhang, X.Y. Sun, F. Wang, J. Wang, Mechanical properties and durability of geopolymer recycled aggregate concrete: A review, Polymers-Basel 15(3) (2023) 615.

[6] K. Korniejenko, P. Kejzlar, P. Louda, The influence of the material structure on the mechanical properties of geopolymer composites reinforced with short fibers obtained with additive technologies, Int J Mol Sci 23(4) (2022) 2023.
[7] Z. Gao, P. Zhang, J.J. Guo, K.X. Wang, Bonding behavior of concrete matrix and alkali-activated mortar incorporating nano-SiO2 and polyvinyl alcohol fiber: Theoretical analysis and prediction model, Ceram Int 47(22) (2021) 31638-31649.
[8] M. Hanumananaik, K.V.L. Subramaniam, Shrinkage in low-calcium fly ash geopolymers for precast applications: Reaction product content and pore structure under drying conditions, J Build Eng 78 (2023) 107583.
[9] A. Fakhrabadi, A.J. Choobbasti, S.S. Kutanaei, Durability evaluation of clayey sandy soil stabilized with copper-slag-based geopolymer under freezing-thawing cycles, Int J Pavement Res T (2023) 1-18.
[10] Z. Azimi, V. Toufigh, Influence of blast furnace slag on pore structure and transport characteristics in low-calcium fly-ash-based geopolymer concrete, Sustainability-Basel 15(18) (2023) 13348.
[11] F. Hong, S. Yu, D.S. Hou, Z.J. Li, H.W. Sun, P. Wang, M.H. Wang, Study on the mechanical properties, gelling products and alkalization process of alkali-activated metakaolin: From experiment to molecular dynamics simulation, J Build Eng 79 (2023) 107705.
[12] T. Luukkonen, Z. Abdollahnejad, J. Yliniemi, P. Kinnunen, M. Illikainen, One-part alkali-activated materials: A review, Cement Concrete Res 103 (2018) 21-34.
[13] T.W. Cheng, J.P. Chiu, Fire-resistant geopolymer produced by granulated blast furnace slag, Miner Eng 16(3) (2003) 205-210.
[14] W.L. Tu, M.Z. Zhang, Behaviour of alkali-activated concrete at elevated temperatures: A critical review, Cement Concrete Comp 138 (2023) 104961.
[15] C.L. Chan, M.Z. Zhang, Behaviour of strain hardening geopolymer composites at elevated temperatures, Cement Concrete Comp 132 (2022) 104634.
[16] W.L. Tu, G.H. Fang, B.Q. Dong, Y.K. Hu, M.Z. Zhang, Behaviour of alkali-activated fly ash-slag paste at elevated temperatures: An experimental study, Cement Concrete Comp 147 (2024) 105438.
[17] Y. Luo, S.H. Li, K.M. Klima, H.J.H. Brouwers, Q.L. Yu, Degradation mechanism of hybrid fly ash/slag based geopolymers exposed to elevated temperatures, Cement Concrete Res 151 (2022) 106649.
[18] R.J. Cai, H.L. Ye, Clinkerless ultra-high strength concrete based on alkali-activated slag at high temperatures, Cement Concrete Res 145 (2021) 106465.

[19] Z. Pan, J.G. Sanjayan, B.V. Rangan, An investigation of the mechanisms for strength gain or loss of geopolymer mortar after exposure to elevated temperature, J Mater Sci 44(7) (2009) 1873-1880.
[20] Z. Pan, J.G. Sanjayan, F. Collins, Effect of transient creep on compressive strength of geopolymer concrete for elevated temperature exposure, Cement Concrete Res 56 (2014) 182-189.
[21] M. Chen, Z. Sun, W. Tu, X. Yan, M. Zhang, Behaviour of recycled tyre polymer fibre reinforced concrete at elevated temperatures, Cement and Concrete Composites (2021) 104257.
[22] F.L. Qu, W.G. Li, Z. Tao, A. Castel, K.J. Wang, High temperature resistance of fly ash/GGBFS-based geopolymer mortar with load-induced damage, Mater Struct 53(4) (2020) 1-21.
[23] P. Behera, V. Baheti, J. Militky, S. Naeem, Microstructure and mechanical properties of carbon microfiber reinforced geopolymers at elevated temperatures, Constr Build Mater 160 (2018) 733-743.
[24] Z. Pan, Z. Tao, Y.F. Cao, R. Wuhrer, T. Murphy, Compressive strength and microstructure of alkali-activated fly ash/slag binders at high temperature, Cement Concrete Comp 86 (2018) 9-18.
[25] W.L. Tu, G.H. Fang, B.Q. Dong, M.Z. Zhang, Multiscale study of microstructural evolution in alkali-activated fly ash-slag paste at elevated temperatures, Cement Concrete Comp 143 (2023) 105258.
[26] G. Fang, Multiscale characterisation of microstructure and mechanical properties of alkali-activated fly ash-slag concrete, PhD Thesis, UCL (University College London), 2021.
[27] R.J. Thomas, B.S. Gebregziabiher, A. Giffin, S. Peethamparan, Micromechanical properties of alkali-activated slag cement binders, Cement Concrete Comp 90 (2018) 241-256.
[28] J. Nemecek, V. Smilauer, L. Kopecky, Nanoindentation characteristics of alkali-activated aluminosilicate materials, Cement Concrete Comp 33(2) (2011) 163-170.
[29] H. Lee, V. Vimonsatit, P. Chindaprasirt, Mechanical and micromechanical properties of alkali activated fly-ash cement based on nano-indentation, Constr Build Mater 107 (2016) 95-102.
[30] Y. Ma, G. Ye, J. Hu, Micro-mechanical properties of alkali-activated fly ash evaluated by nanoindentation, Constr Build Mater 147 (2017) 407-416.
[31] F. Puertas, M. Palacios, H. Manzano, J.S. Dolado, A. Rico, J. Rodríguez, A model for the C-A-S-H gel formed in alkali-activated slag cements, J Eur Ceram Soc 31(12) (2011) 2043-2056.
[32] G.H. Fang, M.Z. Zhang, Multiscale micromechanical analysis of alkali-activated fly ash-slag paste, Cement Concrete Res 135 (2020) 105860.
[33] G.H. Fang, W.K. Ho, W.L. Tu, M.Z. Zhang, Workability and mechanical properties of alkali-activated fly ash-slag concrete cured at ambient temperature, Constr Build Mater 172 (2018) 476-487.
[34] G.H. Fang, M.Z. Zhang, The evolution of interfacial transition zone in alkali-activated fly ash-slag concrete, Cement Concrete Res 129 (2020) 105963.

[35] H. Zhong, M.Z. Zhang, Effect of recycled tyre polymer fibre on engineering properties of sustainable strain hardening geopolymer composites, Cement Concrete Comp 122 (2021) 104167.
[36] A. Committee, Building code requirements for structural concrete (ACI 318-08) and commentary, American Concrete Institute, 2008.
[37] J.R. Ren, H.G. Chen, T. Sun, H. Song, M.S. Wang, Flexural Behaviour of Combined FA/GGBFS Geopolymer Concrete Beams after Exposure to Elevated Temperatures, Adv Mater Sci Eng 2017 (2017) 6854043.
[38] J.R. Ren, H.G. Chen, R.X. Dai, T. Sun, Behavior of combined fly ash/GBFS-based geopolymer concrete after exposed to elevated temperature, 2019 3rd International Workshop on Renewable Energy and Development (Iwred 2019) 267 (2019) 032056.
[39] S.M. Park, J.G. Jang, N.K. Lee, H.K. Lee, Physicochemical properties of binder gel in alkali-activated fly ash/slag exposed to high temperatures, Cement Concrete Res 89 (2016) 72-79.
[40] N.K. Lee, K.T. Koh, G.H. An, G.S. Ryu, Influence of binder composition on the gel structure in alkali activated fly ash/slag pastes exposed to elevated temperatures, Ceram Int 43(2) (2017) 2471-2480.
[41] J.Y. Ye, W.S. Zhang, D. Shi, Effect of elevated temperature on the properties of geopolymer synthesized from calcined ore-dressing tailing of bauxite and ground-granulated blast furnace slag, Constr Build Mater 69 (2014) 41-48.
[42] X.H. Zhu, X.J. Kang, J.X. Deng, K. Yang, L.W. Yu, C.H. Yang, A comparative study on shrinkage characteristics of graphene oxide (GO) and graphene nanoplatelets (GNPs) modified alkali-activated slag cement composites, Mater Struct 54(3) (2021).
[43] G.H. Fang, Q. Wang, M.Z. Zhang, In-situ X-ray tomographic imaging of microstructure evolution of fly ash and slag particles in alkali-activated fly ash-slag paste, Compos Part B-Eng 224 (2021) 109221.
[44] G.H. Fang, Q. Wang, M.Z. Zhang, Micromechanical analysis of interfacial transition zone in alkali-activated fly ash-slag concrete, Cement Concrete Comp 119 (2021) 103990.
[45] N.D. Jiang, Z. Ge, Z.Y. Wang, T.M. Gao, H.Z. Zhang, Y.F. Ling, B. Savija, Size effect on compressive strength of foamed concrete: Experimental and numerical studies, Mater Design 240 (2024) 112841.
[46] I. Hager, M. Sitarz, K. Mróz, Fly-ash based geopolymer mortar for high-temperature application - Effect of slag addition, J Clean Prod 316 (2021) 128168.
[47] H. Liu, W. Jing, L.L. Qin, P. Duan, Z.H. Zhang, R. Guo, W.L. Li, Thermal stability of geopolymer modified by different silicon source materials prepared from solid wastes, Constr Build Mater 315 (2022) 125709.

[48] B. Kanagaraj, N. Anand, R.S. Raj, E. Lubloy, Behavioural studies on binary blended high strength self compacting geopolymer concrete exposed to standard fire temperature, Ain Shams Eng J 15(2) (2024) 102394.
[49] X. Jiang, Y.Y. Zhang, R. Xiao, P. Polaczyk, M.M. Zhang, W. Hu, Y. Bai, B.S. Huang, A comparative study on geopolymers synthesized by different classes of fly ash after exposure to elevated temperatures, J Clean Prod 270 (2020) 122500.
[50] A. Fernandez-Jimenez, J.Y. Pastor, A. Martin, A. Palomo, High-temperature resistance in alkali-activated cement, J Am Ceram Soc 93(10) (2010) 3411-3417.
[51] C. Li, H.H. Sun, L.T. Li, A review: The comparison between alkali-activated slag (Si plus Ca) and metakaolin (Si plus Al) cements, Cement Concrete Res 40(9) (2010) 1341-1349.
[52] M.J.A. Qomi, F.J. Ulm, R.J.M. Pellenq, Evidence on the dual nature of aluminum in the Calcium-Silicate-Hydrates based on atomistic simulations, J Am Ceram Soc 95(3) (2012) 1128-1137.
[53] P. Faucon, J.M. Delaye, J. Virlet, J.F. Jacquinot, F. Adenot, Study of the structural properties of the C-S-H(I) by molecular dynamics simulation, Cement Concrete Res 27(10) (1997) 1581-1590.
[54] S. Merlino, E. Bonaccorsi, T. Armbruster, The real structure of tobermorite 11 angstrom: normal and anomalous forms, OD character and polytypic modifications, Eur J Mineral 13(3) (2001) 577-590.
[55] I. Ismail, S.A. Bernal, J.L. Provis, R.S. Nicolas, S. Hamdan, J.S.J. van Deventer, Modification of phase evolution in alkali-activated blast furnace slag by the incorporation of fly ash, Cement Concrete Comp 45 (2014) 125-135.
[56] I. Garcia-Lodeiro, A. Palomo, A. Fernandez-Jimenez, D.E. Macphee, Compatibility studies between N-A-S-H and C-A-S-H gels. Study in the ternary diagram Na2O-CaO-Al2O3-SiO2-H2O, Cement Concrete Res 41(9) (2011) 923-931.
[57] H.L. Ye, A. Radlinska, Fly ash-slag interaction during alkaline activation: Influence of activators on phase assemblage and microstructure formation, Constr Build Mater 122 (2016) 594-606.
[58] M.R. Ahmad, L.P. Qian, Y. Fang, A.G. Wang, J.G. Dai, A multiscale study on gel composition of hybrid alkali-activated materials partially utilizing air pollution control residue as an activator, Cement Concrete Comp 136 (2023) 104856.
[59] J.S.J. van Deventer, R.S. Nicolas, I. Ismail, S.A. Bernal, D.G. Brice, J.L. Provis, Microstructure and durability of alkali-activated materials as key parameters for standardization, J Sustain Cem-Based 4(2) (2015) 116-128.
[60] Y. Luo, H.J.H. Brouwers, Q.L. Yu, Understanding the gel compatibility and thermal behavior of alkali activated Class F fly ash/ladle slag: The underlying role of Ca availability, Cement Concrete Res 170 (2023) 107198.

[61] B. Walkley, R. San Nicolas, M.A. Sani, G.J. Rees, J.V. Hanna, J.S.J. van Deventer, J.L. Provis, Phase evolution of C-(N)-A-S-H/N-A-S-H gel blends investigated via alkali-activation of synthetic calcium aluminosilicate precursors, Cement Concrete Res 89 (2016) 120-135.
[62] I. García-Lodeiro, A. Fernández-Jiménez, A. Palomo, Variation in hybrid cements over time. Alkaline activation of fly ash-portland cement blends, Cement Concrete Res 52 (2013) 112-122.
[63] I. García-Lodeiro, A. Fernández-Jiménez, A. Palomo, D.E. Macphee, Effect of calcium additions on N-A-S-H cementitious gels, J Am Ceram Soc 93(7) (2010) 1934-1940.
[64] X.H. Zhu, I.G. Richardson, Morphology-structural change of C-A-S-H gel in blended cements, Cement Concrete Res 168 (2023) 107156.
[65] P.M. Ashraf, S.N. Thomas, L. Edwin, Development of graphene-nanometre-sized cerium oxide-incorporated aluminium and its electrochemical evaluation, Appl Nanosci 6(2) (2016) 149-158.
[66] M. Miller, C. Bobko, M. Vandamme, F.J. Ulm, Surface roughness criteria for cement paste nanoindentation, Cement Concrete Res 38(4) (2008) 467-476.
[67] L. Sadowski, D. Stefaniuk, A. Zak, K.J. Krakowiak, Micromechanical properties within the interphase between heterogeneous layers made of cementitious composites, Constr Build Mater 215 (2019) 1033-1043.
[68] C.L. Hu, Z.J. Li, A review on the mechanical properties of cement-based materials measured by nanoindentation, Constr Build Mater 90 (2015) 80-90.
[69] Z.Y. Luo, W.G. Li, Y.X. Gan, K. Mendu, S.P. Shah, Applying grid nanoindentation and maximum likelihood estimation for N-A-S-H gel in geopolymer paste: Investigation and discussion, Cement Concrete Res 135 (2020) 106112.
[70] M. Nedeljkovic, B. Savija, Y.B. Zuo, M. Lukovic, G. Ye, Effect of natural carbonation on the pore structure and elastic modulus of the alkali-activated fly ash and slag pastes, Constr Build Mater 161 (2018) 687-704.
[71] R.T. Chancey, P. Stutzman, M.C.G. Juenger, D.W. Fowler, Comprehensive phase characterization of crystalline and amorphous phases of a Class F fly ash, Cement Concrete Res 40(1) (2010) 146-156.
[72] S. Puligilla, P. Mondal, Role of slag in microstructural development and hardening of fly ash-slag geopolymer, Cement Concrete Res 43 (2013) 70-80.
[73] O. Burciaga-Diaz, J.I. Escalante-Garcia, Comparative performance of alkali activated slag/metakaolin cement pastes exposed to high temperatures, Cement Concrete Comp 84 (2017) 157-166.
[74] L.P. Liu, H.N. Liu, Y. Xu, J.C. Xiang, Y. He, G.J. Zheng, Mechanical properties and microstructure of alkali-activated slag grouting materials exposed to flowing $NaHCO_3$ solution, J Mater Civil Eng 34(12) (2022) 04022332.

[75] I. Zafar, K. Rashid, R. Hameed, K. Aslam, Correlating reactivity of fly ash with mechanical strength of the resultant geopolymer, Arab J Sci Eng 47(10) (2022) 12469-12478.
[76] C. Kuenzel, N. Ranjbar, Dissolution mechanism of fly ash to quantify the reactive aluminosilicates in geopolymerisation, Resour Conserv Recy 150 (2019) 104421.
[77] I. Garcia-Lodeiro, A. Palomo, A. Fernández-Jiménez, An overview of the chemistry of alkali-activated cement-based binders, Handbook of alkali-activated cements, mortars and concretes (2015) 19-47.
[78] Z.Q. Sun, A. Vollpracht, Isothermal calorimetry and in-situ XRD study of the NaOH activated fly ash, metakaolin and slag, Cement Concrete Res 103 (2018) 110-122.
[79] A. Palomo, P. Krivenko, I. Garcia-Lodeiro, E. Kavalerova, O. Maltseva, A. Fernandez-Jimeneza, A review on alkaline activation: new analytical perspectives, Mater Construcc 64(315) (2014) 22.
[80] Y. Li, Material properties and explosive spalling of ultra-high performance concrete in fire. (Thesis), (2018).
[81] W.L. Tu, M.Z. Zhang, Multiscale microstructure and micromechanical properties of alkali-activated concrete: A critical review, Cement Concrete Comp 152 (2024) 105664.
[82] P. Duxson, J.L. Provis, G.C. Lukey, S.W. Mallicoat, W.M. Kriven, J.S.J. van Deventer, Understanding the relationship between geopolymer composition, microstructure and mechanical properties, Colloid Surface A 269(1-3) (2005) 47-58.
[83] W.L. Tu, Y. Zhu, G.H. Fang, X.G. Wang, M.Z. Zhang, Internal curing of alkali-activated fly ash-slag pastes using superabsorbent polymer, Cement Concrete Res 116 (2019) 179-190.
[84] H.G. Zhang, L. Li, C. Yuan, Q.Y. Wang, P.K. Sarker, X.S. Shi, Deterioration of ambient-cured and heat-cured fly ash geopolymer concrete by high temperature exposure and prediction of its residual compressive strength, Constr Build Mater 262 (2020) 120924.
[85] A. Behnood, M. Ghandehari, Comparison of compressive and splitting tensile strength of high-strength concrete with and without polypropylene fibers heated to high temperatures, Fire Safety J 44(8) (2009) 1015-1022.
[86] G.R. Consolazio, M. McVay, J. Rish III, Measurement and prediction of pore pressure in cement mortar subjected to elevated temperature, Proceedings of the International Workshop on Fire Performance of High-Strength Concrete, NIST, Gaithersburg, Maryland, 1997, pp. 125-148.
[87] I. Abdulkadir, B.S. Mohammed, A.M. Al-Yacouby, E.L. Woen, T. Tafsirojjaman, Tailoring an engineered cementitious composite with enhanced mechanical performance at ambient and elevated temperatures using graphene oxide and crumb rubber, J Mater Res Technol 28 (2024) 4508-4530.